Applied Thermal Engineering 179 (2020) 115692

Contents lists available at ScienceDirect

Applied Thermal Engineering

journal homepage: www.elsevier.com/locate/apthermeng

Numerical simulation of thermal response behavior of floating-roof tanks exposed to pool fire

Xiuzhen Wang[a,c,d], Kuibin Zhou[a,*], Ahmed Mebarki[a,b,1], Juncheng Jiang[a]

[a] Jiangsu Key Laboratory of Hazardous Chemicals Safety and Control, College of Safety Science and Engineering, Nanjing Tech University, Nanjing, 211816, Jiangsu, China
[b] University Gustave Eiffel, Laboratory Multi Scale Modeling and Simulation (MSME UMR 8208 UGE/UPEC/CNRS), 5 Bd Descartes, 77454 Marne-La-Vallée, France
[c] Key Laboratory of Microgravity, Institute of Mechanics, Chinese Academy of Sciences, Beijing 100190, China
[d] School of Engineering Science, University of Chinese Academy of Sciences, Beijing 100049, China

HIGHLIGHTS

- Theoretical framework is built for thermal response behavior of tank exposed to fire.
- Assumption of constant thermo-physical property of liquid in tank is reasonable.
- Non-uniform distribution of heat flux on the tank surface holds a significant effect.
- Failure time of tank increases as the thermal diffusivity of liquid in tank increases.

ARTICLE INFO

Keywords:
Thermal response
Radiant heat
Pool fire
Storage tank
Numerical simulation

ABSTRACT

In industrial plants, the fire spread of separative fuel tanks could be related to the tank rupture caused by the thermal radiation from nearby fires. The present paper develops a theoretical framework for analyzing the thermal response behavior and failure time of floating-roof atmospheric storage tanks when exposed to a pool fire. Multi-layer cylindrical flame radiation model is used to predict the radiant heat flux field on the surface of tanks. This radiant heat, considered as the thermal load for a finite element analysis (FEA), influences the tank transient response under thermo-mechanical coupling effects. The paper investigates the respective and combined effects of the tank thermo-physical properties, the non-uniform radiant heat flux distribution, the generated stress as well as the failure time of target tank. For comparative purposes, an empty tank is used as a reference. The results show that the empty and full-filled storage tanks differ in their thermal response modes and their thermos-mechanical behaviors. Within the values in the temperature range of interest adopted for the tank thermo-physical properties, their variations with the temperature have little influence on the tanks' behavior. The non-uniform radiant heat along the vertical and around circumferential directions of tank has a significant effect on the tanks' behavior. The stored liquid mediums considerably affect the tanks' behavior. The failure time of empty tank is over three times as long as that of full-filled storage tank.

1. Introduction

Storage tank farms may contain a number of tanks within a closely space. If a fire occurs in any of the tanks, the surrounding tanks might be easily ignited or damaged. In the past decades, such accidents generated great hazardous heat, impacting nearby occupants and facilities and resulting in great economic loss [1–5]. Chang and Lin [3] reviewed 242 tank accidents occurred in industrial facilities from 1965 to 2005, finding that 85% of the accidents were initiated by fire and explosion. A survey has shown that pool fire is the most frequent cause among the domino events initiated by fires [2].

Oil storage tanks roof can be divided into fixed-roof and floating-roof [6,7]. The fixed-roof can be subdivided into conical-roof and flat-roof, and the floating-roof can be subdivided into outer floating-roof and inner floating-roof. Several studies have investigated the storage tank fire accidents [7–18] and the thermal response of heated storage tanks [4,19–23]. Some numerical studies, using finite element code of Abaqus [4,19,20,22] or Ansys [21], have particularly addressed the

* Corresponding author.
E-mail address: kbzhou@njtech.edu.cn (K. Zhou).
[1] Guest Professor at Nanjing Tech University, within "High-Level Foreign Talents Programme" grant.

https://doi.org/10.1016/j.applthermaleng.2020.115692
Received 25 January 2020; Received in revised form 26 April 2020; Accepted 1 July 2020
Available online 06 July 2020
1359-4311/

Nomenclature

$c_{P,\infty}(c_p)$	constant pressure specific capacity (kJ/(kg·K))
c	the coefficient ranging from 1.20 to 1.33
C_t	the specific heat of target tank (kJ/(kg·K))
$[C^t]$	the element thermal damping matrix
$[C]$	the damping matrix
d_t	the wall thickness of target tank (m)
D	the pool diameter (m)
E_f	event corresponding to the tank failure
$E_{T_{cr}}$	event corresponding to a critical value of the temperature reached either in the stored product or in the tank wall
$E_{\sigma_{cr}}$	event corresponding to a critical value of the "Von Mises" equivalent stress reached at any part of the tank
$E_{d_{cr}}$	event corresponding to a critical value of the longitudinal or circumferential displacement reached at any part of the tank
$E_{Tcr\|\mathrm{wall}}$	event corresponding to a critical value of the temperature reached in the tank wall
$E_{Tcr\|\mathrm{prod}}$	event corresponding to a critical value of the temperature reached within the stored product
$\{F^{nd}\}$	the applied nodal force vector
$\{F^{th}\}$	the element thermal load vector
$\{F^{pr}\}$	the element pressure vector
$\{F^{ac}\}$	the force vector due to acceleration effects
g	acceleration of gravity (m/s^2)
h_t	the vertical distance of the target point above the fuel surface (m)
h	the convection heat transfer coefficient between target tank and ambient air (W/(m^2·°C))
H_c	the continuous flame height (m)
H_i	the intermittent flame height (m)
$H_{j\text{-}1}$	the total flame height of (j-1) layers (m)
ΔH_c	combustion heat (kJ/mol)
ΔH	each layer height (m)
H	average flame height (m)
k	the mean absorption-emission coefficient of the flame
$[K]$	the stiffness matrix
$[K^{tb}]$	the element diffusion conductivity matrix
$[K^{tc}]$	element convection surface conductivity matrix
l_{m}	the mean optical path length of the whole flame volume (m)
L	horizontal distance of the target points away from the fire plume centerline (m)
$\dot{m}''(\dot{m}''_\infty)$	(maximum) mass loss rate per area (kg/(m^2·s))
$[M]$	the mass matrix
n	the total layer number
$\dot{q}''_{\mathrm{F}\to\mathrm{T}}(\dot{q}_t'')$	radiant heat flux (kW/m^2)
$\dot{Q}^*$	dimensionless heat release rate
$\{Q^{nd}\}$	the applied nodal heat flow rate vector
$\{Q^g\}$	the element heat generation load
$\{Q^c\}$	the element convection surface heat flow vector
$\dot{Q}$	heat release rate (kW)
t	time (s)
T_∞	ambient air temperature, 293 K
T_0	centerline temperature (K)
T_f	the flame centerline temperature (K)
T_{fj}	the flame temperature of the jth layer (K)
T_T	the temperature of target tank (K)
$\{\ddot{T}\}$	the second time derivative of temperature vector
$\{\dot{T}\}$	the time derivative of temperature
$\{T\}$	the temperature vector
$\{\ddot{u}\}$	the acceleration vector
$\{\dot{u}\}$	the time derivative of displacement vector
$\{u\}$	displacement vector
z	the vertical distance of the jth layer flame above the liquid fuel surface or gas burner exit (m)

Greek symbols

α	the angle between the y axis and the horizontal line of the target to the pool fire centerline
β	a mean-beam-length corrector
Δ	the difference between the intermittent flame height and the continuous flame height
ε	flame emissivity
ε_T	the emissivity of target tank
ν	Poisson ratio
ρ_T	the density of target tank (kg/m^3)
ρ_∞	ambient air density (kg/m^3)
ρ_f	the density of medium in the target tank (kg/m^3)
σ	Stefan-Boltzman constant, 5.67 × 10^{-8}W/(m^2·K^4)
σ_s^T	the yield strength of steel as a function of temperature
τ	the atmospheric transmissivity to the thermal radiation
χ_e	combustion efficiency
χ_{r}	radiative fraction

Subscripts

f	the flame
fj	the jth layer flame surface
F	the flame surface
T(t)	the target tank
j-1	(j-1) layers of flame

buckling of storage tanks when exposed to the adjacent fire radiation. Zhao et al. [21] used FDS simulation to obtain the temperature field on the surface of heated storage tank, and used afterwards Ansys software to study the failure time. Godoy and Batista [4,19] and Liu [22] used a cosine square function to modulate the temperature in the circumferential direction. Li et al. [20] studied the thermal buckling behavior and failure time of target tank by applying a modified solid flame simulation to estimate the temperature field on target tank surface. Zhang et al. [24] established an integrated probabilistic framework based on the maximum thermal radiation flux received by the target tanks. The thermal response behavior of fixed-roof tanks [7,19,20,22,25,26] has been more intensively studied than tanks with floating-roof [21,24] and open-roof [4,27]. In existing literature, few information is available about the thermal behavior of floating-roof atmospheric storage tanks impacted by adjacent pool fires. It appears therefore a further need to investigate the thermal response of floating-roof heated storage tanks.

Firstly, a multi-layer cylindrical flame radiation model reported in Ref. [28] is used. It aims to accurately calculate the radiant heat flux field on the surface of tanks exposed to pool fires, and the effect of combustion efficiency on the radiant heat flux field is also discussed. Secondly, the temperature versus time predicted by the lumped capacitance method is compared to the numerical result of FEA. Thirdly, the FEA is used to calculate the transient thermal response behavior, including the stress and deformation, for the empty and full-filled tanks. Finally, a comparison between yield strength versus temperature of Q235 steel and the maximum equivalent stress versus time of storage tank is conducted in order to study the failure time of tank. This paper aims to clarify the effects of the tank thermo-physical properties, the non-uniform radiant heat flux distribution and the stored liquid mediums on the thermal response behavior of floating-roof tanks.

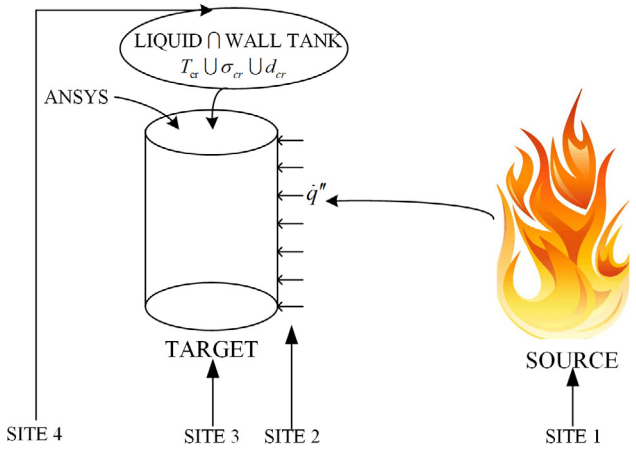

Fig. 1. . Theoretical framework.

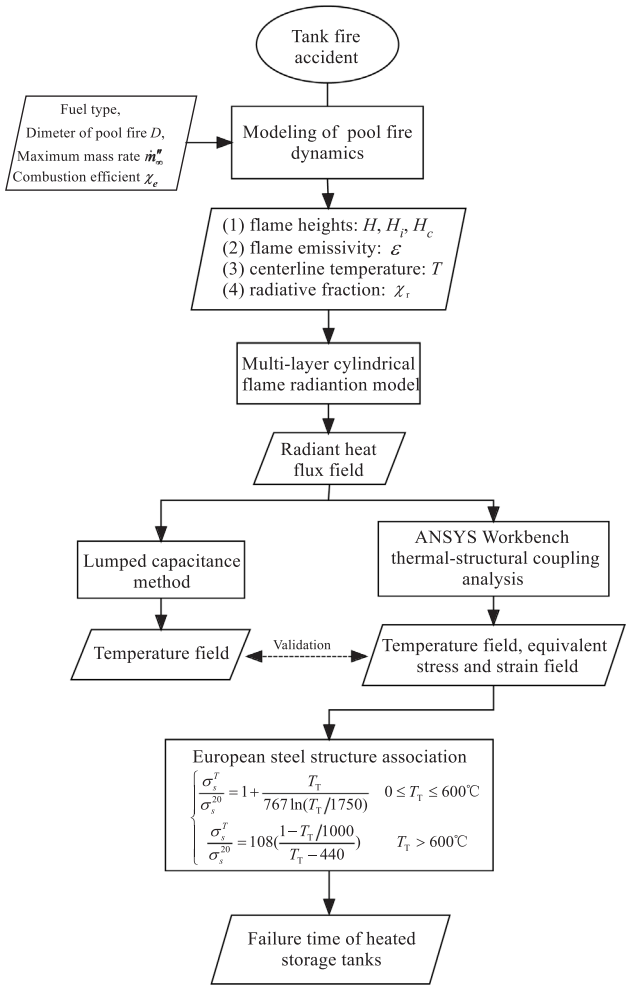

Fig. 2. Global flowchart for thermal failure analysis of target tank.

2. Theoretical framework

As shown in Fig. 1, the initial fire in a so-called "source" tank will affect its neighbors called "target" tanks, and may trigger a secondary sequence of fires or cause the failure of the target tanks. The failure event of target tanks is defined as follows, see Fig. 1:

$$E_f = E_{T_{cr}} \bigcup E_{\sigma_{cr}} \bigcup E_{d_{cr}} \tag{1}$$

where E_f = event corresponding to the tank failure, $E_{T_{cr}}$ = event corresponding to a critical value of the temperature reached either in the stored product or in the tank wall, $E_{\sigma_{cr}}$ = event corresponding to a critical value of the "Von Mises" equivalent stress reached at any part of the tank, $E_{d_{cr}}$ = event corresponding to a critical value of the longitudinal or circumferential displacement reached at any part of the tank, $\cup$ = union symbol for the combination of individual events.

It is worth noting that the critical temperature criterion corresponds to the case where a fire or an explosion can be triggered in the target tank, i.e:

$$E_{T_{cr}} = E_{T_{cr}|\text{wall}} \bigcup E_{T_{cr}|\text{prod}} \tag{2}$$

where $E_{Tcr|\text{wall}}$ and $E_{Tcr|\text{prod}}$ = events corresponding to a critical value of the temperature reached in the tank wall and within the stored product, respectively. $E_{Tcr|\text{prod}}$ can be neglected for the empty tank.

The theoretical framework, proposed in the present paper, consists of modeling of pool fire dynamics, multi-layer cylindrical flame radiation model, lumped capacitance method, thermal-structural coupling analysis and the failure time correlation of heated storage tank. Fig. 2 shows the whole steps required to conduct the thermo-mechanical failure of the target tank, i.e.:

- Define the conditions of the initial fire at the source tank;
- Calculate the thermal effect, i.e. the temperature field in the target tank and inside the stored product;
- Calculate the equivalent Von-Mises stress field in the target tank wall;
- Calculate the maximum (longitudinal and circumferential) displacement field in the target tank.

2.1. Modeling of pool fire dynamics

2.1.1. Model for the flame height

The commonly-used mean flame height formula for pool fire can be written as [29]:

$$H/D = -1.02 + 3.7\dot{Q}^{*0.4} \tag{3}$$

$$\dot{Q}^* = \dot{Q}/(\rho_\infty c_{p,\infty} T_\infty D^2 \sqrt{gD}) \tag{4}$$

$$\dot{Q} = \chi_e \dot{m}'' \pi (D/2)^2 \Delta H_c \tag{5}$$

where H = the mean flame height of pool fire, D = the pool diameter, $\dot{Q}^*$ = the dimensionless heat release rate, $\dot{Q}$ = the actual heat release rate, ρ_∞, $c_{p,\infty}$ and T_∞ = the density, specific heat capacity at constant pressure and temperature of ambient air, respectively, g = the acceleration of gravity, χ_e = combustion efficient that decreases with an increase of pool diameter, $\dot{m}''$ = the mass loss rate per area and ΔH_c = the combustion heat.

The correlation for the difference between the intermittent and continuous flame heights (Δ), can be calculated by [30]:

$$\Delta/H = X(1 - X^2/16)^{0.5}, \quad X = C/\sqrt{H/D} \tag{6}$$

where C = the coefficient ranging from 1.20 to 1.33 (1.27 is arbitrarily adopted in the present paper), The continuous and intermittent flame heights are expressed as $H_c = H - \Delta/2$ and $H_i = H + \Delta/2$, respectively.

2.1.2. Model for the flame emissivity

The flame emissivity of pool fire can be estimated by measurements of transmitted energy from a blackbody radiant source [31–33], whereas the flame is assumed to be an isothermal and homogenous grey emitter with a constant absorption-emission coefficient. Therefore, the flame emissivity is constant within the whole flame volume, i.e.:

$$\varepsilon = 1 - \exp(-kl_m) \tag{7}$$

where k = the mean absorption-emission coefficient of flame, and l_m = the mean optical path length in the whole flame volume, conventionally given by $l_m = \beta D$ where β is a mean-beam-length corrector.

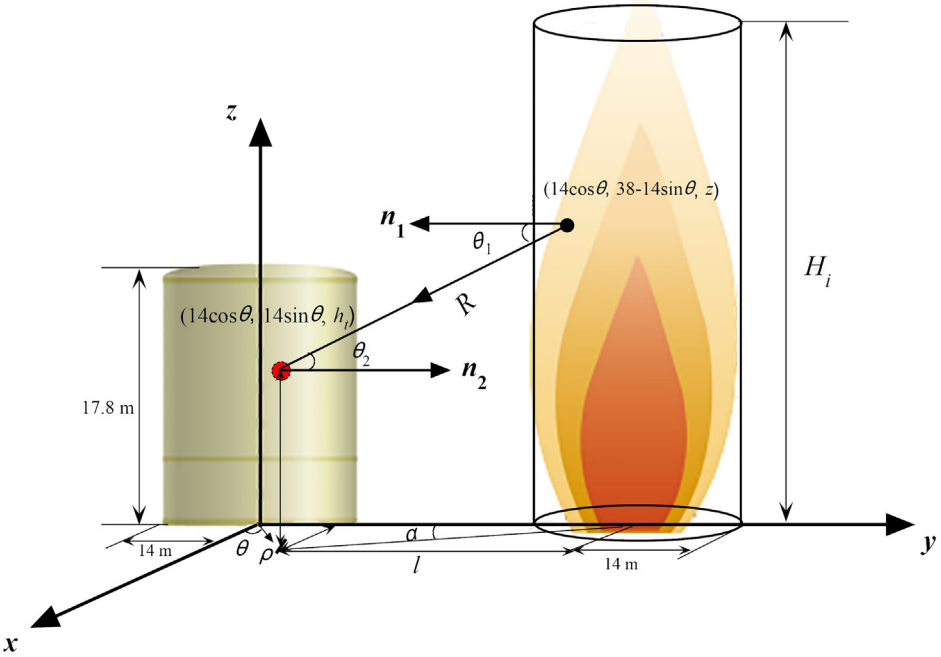

Fig. 3. Layout and radiant heat transfer between pool fire and storage tank.

Table 1
. Thermo-physical properties of gasoline [40].

D (m)	ρ (kg/m^3)	ΔH_c (kJ/kg)	$\dot{m}''_\infty$ (kg/m^2-s)	$\dot{m}''$ (kg/m^2-s)
28	740	43,700	0.055	0.055

Table 2
. Thermo-physical properties of Q235 [41].

T (°C	c_p (J/kg/K)	k (W/(m·K)	$\alpha \times 10^{-5}$ (1/°C)	E (GPa)	ν
25	NA	NA	NA	212	0.288
100	NA	NA	1.20	209	0.291
200	745	61.1	1.26	201	0.294
300	770	55.3	1.33	193	0.288
400	783	48.6	1.39	184	0.283

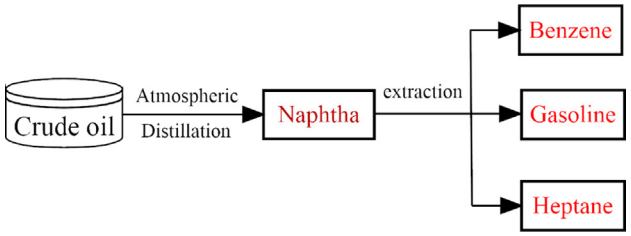

Fig. 4. . flow diagram for crude oil processing.

In general, the mass burning rate of liquid pool fire can be expressed by [34]:

$$\dot{m}'' = \dot{m}''_\infty(1 - \exp(-k\beta D)) \tag{8}$$

where$\dot{m}''_\infty$ = the maximum mass burning rate. Thus, Eq. (7) can reduce to

$$\varepsilon = \dot{m}''/\dot{m}''_\infty \tag{9}$$

2.1.3. Model for radiative fraction

The radiative fraction is defined as the ratio of the total radiant energy emitted from flame versus the total flame heat release rate. The relationship, defined by Yang [35], between the radiative fraction and pool diameter, by analyzing pool fires of different scales, shows that the radiative fraction decreases with increasing pool diameter for large scale pool fires. In addition, the correlation between radiative fraction and pool diameter for heavy hydrocarbon pool fires can be expressed as [36]:

$$\chi_r = 0.35\exp(-0.05D) \tag{10}$$

2.1.4. Model for centerline temperature

The pool fire centerline temperature in the continuous and intermittent flame regions, can be defined as [23,37]:

$$T_f = \begin{cases} T_0 & z \leqslant H_c \\ 293 + (T_0 - 293) \times (H_c/z) & H_c \leqslant z < H_i \end{cases} \tag{11}$$

where$z$ = the vertical distance of the jth layer flame above the fuel surface, T_f = the flame centerline temperature of pool fire, T_0 = the flame centerline temperature in the continuous region.

It is worth noting that the fire temperature can be derived from the energy balance, by integrating the flame surface emissive power over the whole flame surface, which equals the product of the radiative fraction and heat release rate [23]:

$$\oint_s \varepsilon\sigma T_f^4 \mathrm{d}s = \chi_r \times \dot{m}''\pi(D/2)^2\Delta H_c \tag{12}$$

where σ is the Stefan-Boltzman constant (5.67×10^{-8} W/(m^2·K^4)). Note that the definition of radiative fraction is not based on the actual heat release rate but the ideal heat release rate in [36].

2.2. Modeling of thermal radiation from pool fire to target tank

In engineering, the point source model, single cylindrical flame radiation model and multi-layer cylindrical flame radiation model are usually used to predict the thermal radiation of pool fire [23]. The multi-layer cylindrical flame radiation model calculates the radiant heat flux ($\dot{q}''_{F\to T}$) by:

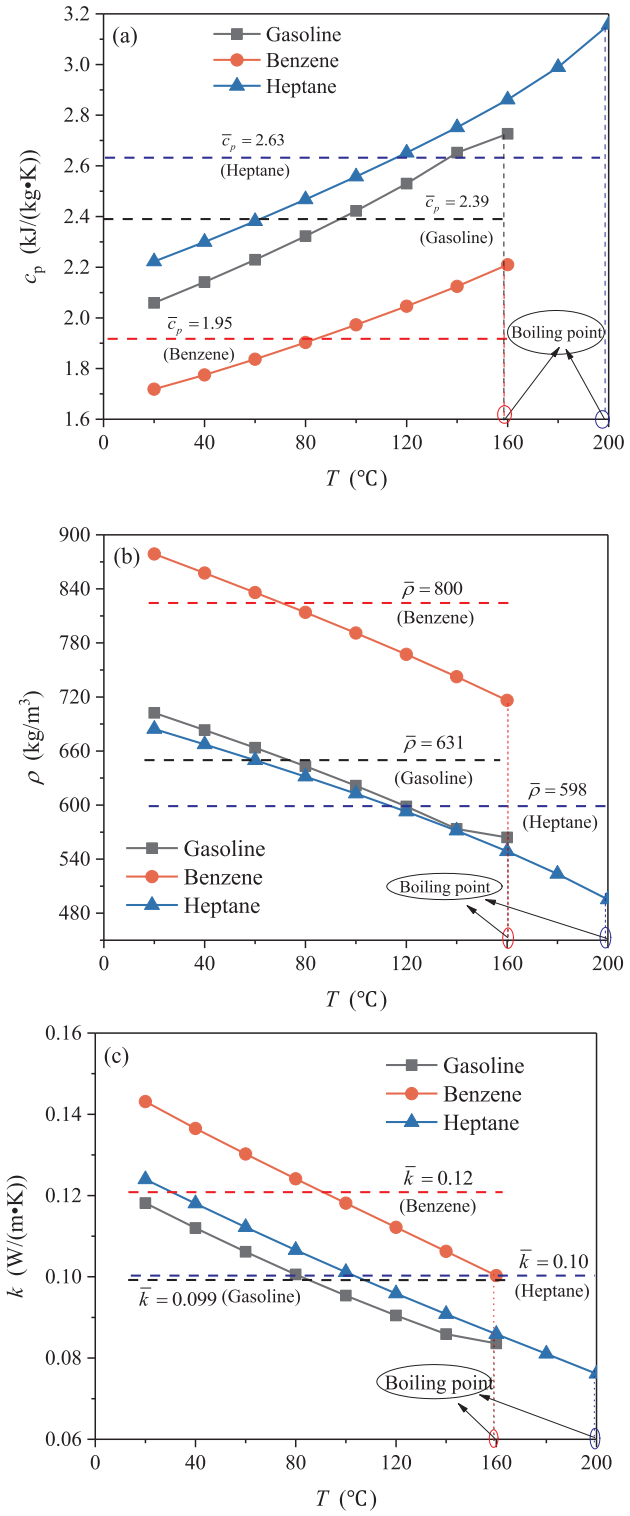

Fig. 5. Thermo-physical properties of liquid medium as a function of temperature: (a) c_p = specific heat; (b) ρ = density; (c) k = thermal conductivity [44].

Table 3
. The flame height for various combustion efficiency.

χ_e	H (m)*	H_i (m)	H_c (m)	T_0 (K)
0.2	7.43	14.65	0.22	3009
0.4	18.93	32.42	5.45	1320
0.6	27.30	43.92	10.67	1114
0.8	34.11	52.90	15.31	1018
1	39.96	60.44	19.48	960

* In calculation of H, the ambient air temperature T_∞ is 293 K, the air density ρ_∞ 1.293 kg/m^3, and the air specific heat $c_{p,\infty}$ 1.004 kJ/(kg K).

$$\dot{q}''_{F\to T} = \sum_{j=1}^{n} \cos\alpha \{\sigma(1 - \exp(-k\beta D)T_{fj}^4 \tau_j \left(\frac{1}{\pi}\int_0^{H_{j-1}+\Delta H} dz \int_0^{\pi} \frac{d(L - d\sin\theta)(L\sin\theta - d)}{[(L^2 - 2dL\sin\theta + d^2) + (h_t - z)^2]^2} d\theta - \frac{1}{\pi}\int_0^{H_{j-1}} dz \int_0^{\pi} \frac{d(L - d\sin\theta)(L\sin\theta - d)}{[(L^2 - 2dL\sin\theta + d^2) + (h_t - z)^2]^2} d\theta \right)\} \quad (13)$$

where j = the jth layer flame, n = the total layer number, α = the angle between the *target surface normal orientation* and the horizontal line of the target point to the pool fire centerline, τ_j = the atmospheric transmissivity to the thermal radiation, T_{fj} = the flame temperature of the jth layer, H_{j-1} = the total flame height of (j-1) layers, h_t = the vertical distance of the target point above the fuel surface, ΔH = the each layer height, and L = the horizontal distance of the target point away from the fire plume centerline. In the present paper, τ_j = 1 and n = 10, as proposed in [23]. Note the angle α within 0 to 90°, and α = 0°as the normal orientation of target surface is perpendicular to the flame centerline, as shown in Fig. 3.

2.3. Lumped capacitance method for calculating the tank surface temperature

In general, the temperature gradient can be neglected within a thin solid such as tank shell. Accordingly, the lumped capacitance method can be used to calculate the temperature versus time of the empty tank exposed to the pool fire. The pool fire radiation heats the tank wall, while the tank wall is cooled by the convective and radiative heat exchange with the surrounding air. As the conduction within the tank wall can be neglected, the heat balance equation can be expressed as [38]:

$$\rho_T c_T d_T \frac{dT_T}{dt} = \dot{q}''_T - 2h(T_T - T_\infty) - 2\varepsilon_T \sigma (T_T^4 - T_\infty^4) \quad (14)$$

where ρ_T, c_T, d_T, T_T and ε_T = the density, specific heat, wall thickness, temperature and emissivity of target tank, respectively, t = the time, $\dot{q}''_T$ = the radiant heat flux received by the target tank, h = the convection heat transfer coefficient between target tank and ambient air, and T_∞ = the ambient air temperature.

2.4. Thermo-mechanical coupling analysis

This paper focuses on the thermal response of the tank in a heated environment, which needs to consider the thermo-mechanical coupling by ANSYS Workbench platform [28]. The transient heat transfer process refers to the heating or cooling process of a system, in which the temperature, heat flow rate, thermal boundary conditions and internal energy of the system change significantly with time. Transient static analysis is used to analyze the response under a given static load, especially the displacement, stress and strain fields of the structure, which are obtained by solving the following system [28]:

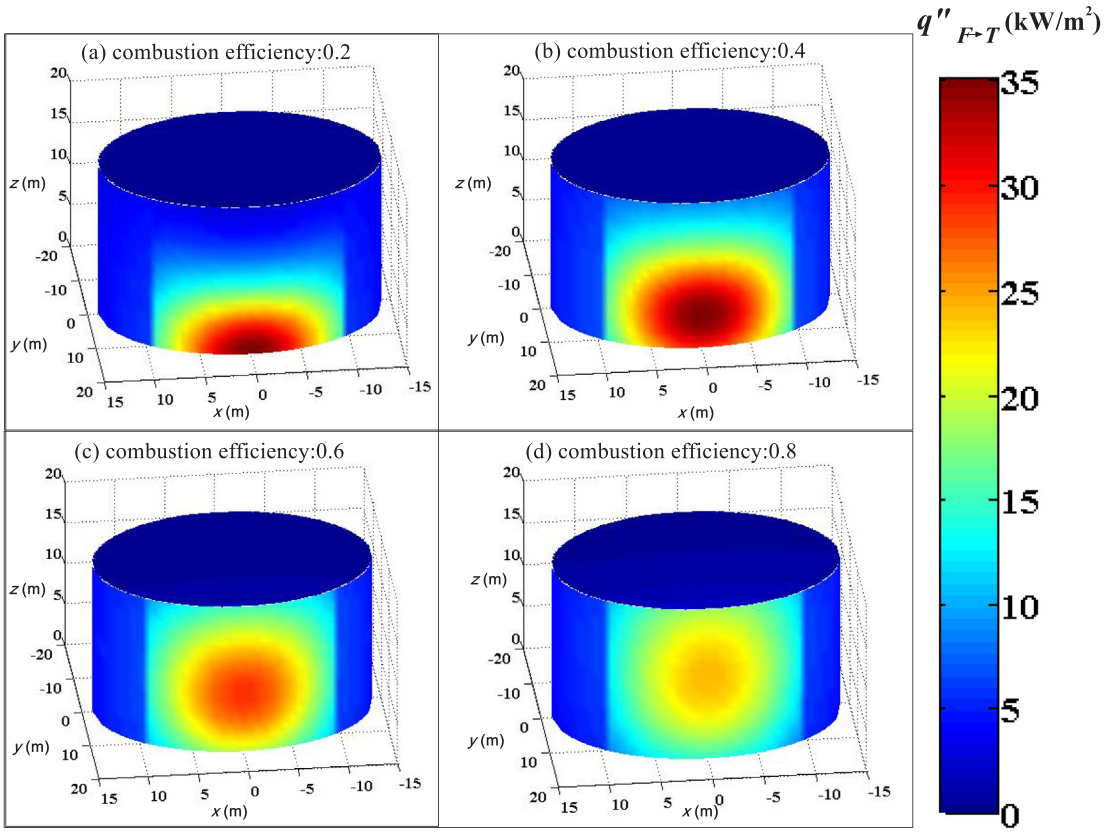

Fig. 6. Radiant heat flux distribution on the surface of target tank.

$$\begin{bmatrix}[M] & [0]\\ [0] & [0]\end{bmatrix}\begin{Bmatrix}\{\ddot{u}\}\\ \{\dot{T}\}\end{Bmatrix}+\begin{bmatrix}[C] & [0]\\ [0] & [C^t]\end{bmatrix}\begin{Bmatrix}\{\dot{u}\}\\ \{\dot{T}\}\end{Bmatrix}+\begin{bmatrix}[K] & [0]\\ [0] & [K^{tb}]+[K^{tc}]\end{bmatrix}\begin{Bmatrix}\{u\}\\ \{T\}\end{Bmatrix}=\begin{Bmatrix}\{F^{nd}\}+\{F^{th}\}+\{F^{pr}\}+\{F^{ac}\}\\ \{Q^{nd}\}+\{Q^g\}+\{Q^c\}\end{Bmatrix} \quad (15)$$

where $[M]$= the mass matrix, $\{\ddot{u}\}$=the acceleration vector, $\{\dot{T}\}$ = the second time derivative of temperature vector, $[C]$ = the damping matrix, $[C^t]$ = the element thermal damping matrix, $\{\dot{u}\}$ = the velocity vector, $\{\dot{T}\}$ = the time derivative of temperature, $[K]$ = the stiffness matrix, $[K^{tb}]$ = the element diffusion conductivity matrix, $[K^{tc}]$ = element convection surface conductivity matrix, $\{u\}$ = displacement vector, $\{T\}$ = the temperature vector, $\{F^{nd}\}$ = the applied nodal force vector, $\{F^{th}\}$ = the element thermal load vector, $\{F^{pr}\}$ = the element pressure vector, $\{F^{ac}\}$ = the force vector due to acceleration effects, $\{Q^{nd}\}$ = the applied nodal heat flow rate vector, $\{Q^g\}$ = the element heat generation load and $\{Q^c\}$ = the element convection surface heat flow vector.

2.5. Model for failure time of target tank

In the fire radiation heating condition, the outer floating-roof tank could fail due to either the boiling of storage liquid medium or the thermal rupture of tank shell. If the liquid medium boils, much vapor will escape through the automatic venting valve and mixes with the outside air. Accordingly, secondary fire and explosion are likely to occur. The increasing temperature can also cause a decrease of the yield strength of tank shell, and an increase of the thermal stress. When the stress (equivalent Von Mises stress) reaches the yield strength, the tank will be failed by mechanical rupture. In short, there are two main failure modes. The failure time of target tank is the minimum one of two failure modes. The target tank can also fail due to elastic buckling in either longitudinal or circumferential modes. However, the buckling is not considered in the present paper, for the sake of simplicity.

For the failure mode of thermal rupture, the European Steel Structure Association (ECCS) has conducted a large number of experimental measurements, and gave the correlation of the yield strength of steel under different temperatures [39]:

$$\begin{cases}\frac{\sigma_s^T}{\sigma_s^{20}}=1+\frac{T_T}{767\ln(T_T/1750)} & 0\leqslant T_T\leqslant 600°C\\ \frac{\sigma_s^T}{\sigma_s^{20}}=108(\frac{1-T_T/1000}{T_T-440}) & T_T>600°C\end{cases} \quad (16)$$

where: σ_s^T is the yield strength of steel as a function of temperature (T_T). In particular, σ_s^{20}equals 235 MPa for Q235 steel.

3. Model setup and boundary conditions

Fig. 3 presents the layout of pool fire and outer floating-roof storage tank, as well as the radiant heat transfer between them. For illustrative purposes, the horizontal distance between the central axis of pool fire and storage tank is 38 m, and the pool fire diameter is 28 m, and the target tank, made of carbon steel (Q235), holds the diameter of 28 m, the height of 17.8 m and the wall thickness of 12 mm. Note that the multi-layer flame cylindrical radiation model does not consider the smoke around the flame. Thus, the model would give an underestimation of radiant heat flux, due to the radiation blockage of a lot of smoke produced by large pool fires.

3.1. Physico-chemical properties of pool fire

For illustrative purposes, the gasoline pool fire is considered to occur within the tank farm, with the thermos-physical properties listed in Table 1. The development of pool fire can be divided into growth, steady and decay phases, respectively. However, the present study focuses only on the steady phase in which the pool fire holds a quasi-steady flame height.

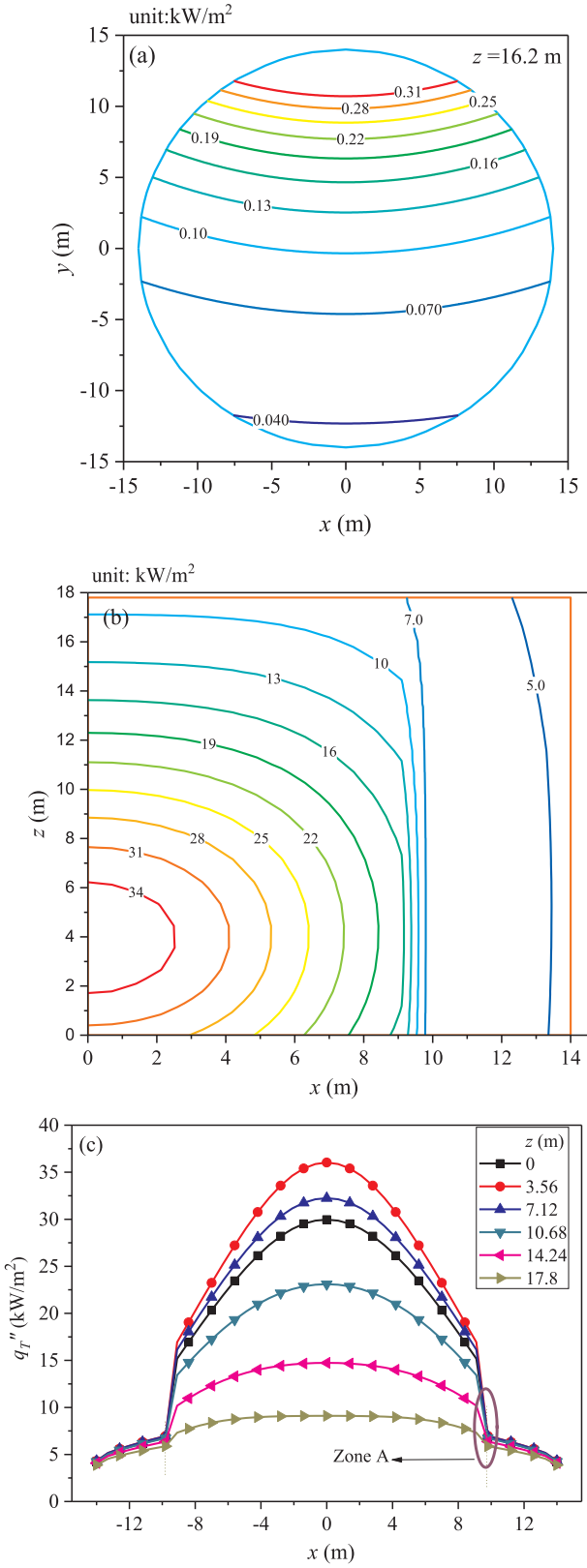

Fig. 7. Radiant heat flux distribution on the target tank surface: (a) on the top roof, (b) in the vertical and (c) circumferential directions.

3.2. Properties of Q235 steel

The physical and mechanical properties of Q235 steel are a considerable function of temperature. Table 2 lists the specific heat at constant pressure, thermal conductivity, thermal expansion coefficient, elastic modulus and Poisson ratio of Q235 steel at different elevated temperatures. However, the density equals 7860 kg/m^3, despite the temperature. The convective heat transfer coefficient, between the tank wall and the surrounding air, is considered to equal 5 W/(m^2·°C), while it is 50 W/(m^2·°C) between the tank wall and the storage liquid medium.

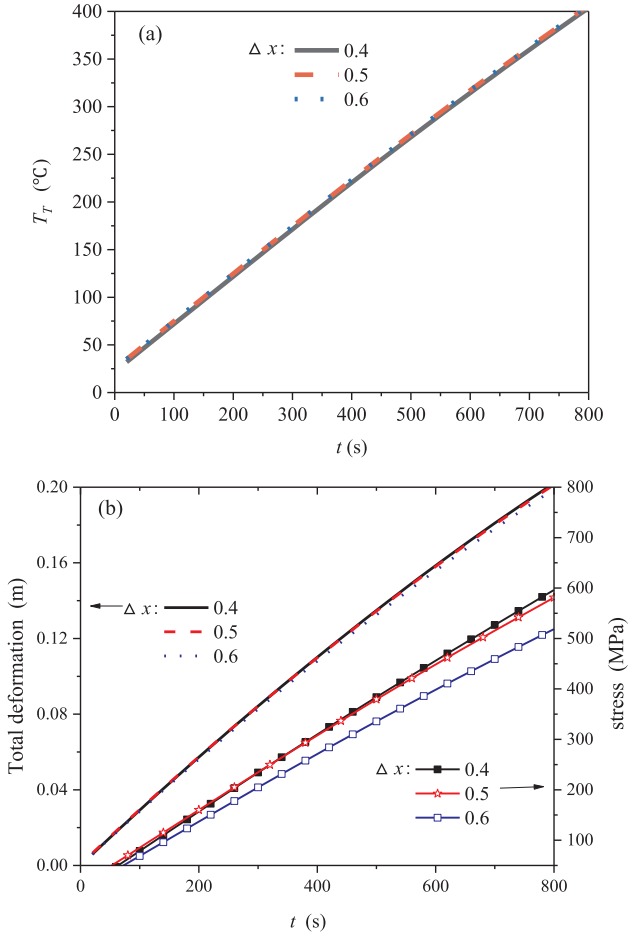

Fig. 8. . Effect of grid size on the simulation results: (a) maximum temperature versus time, (b) maximum total deformation and stress versus time.

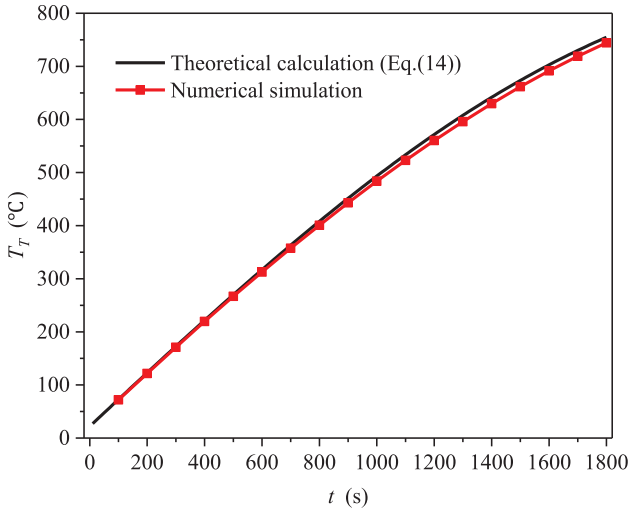

Fig. 9. Variation of temperature versus time at the point where maximum radiant heat flux locates.

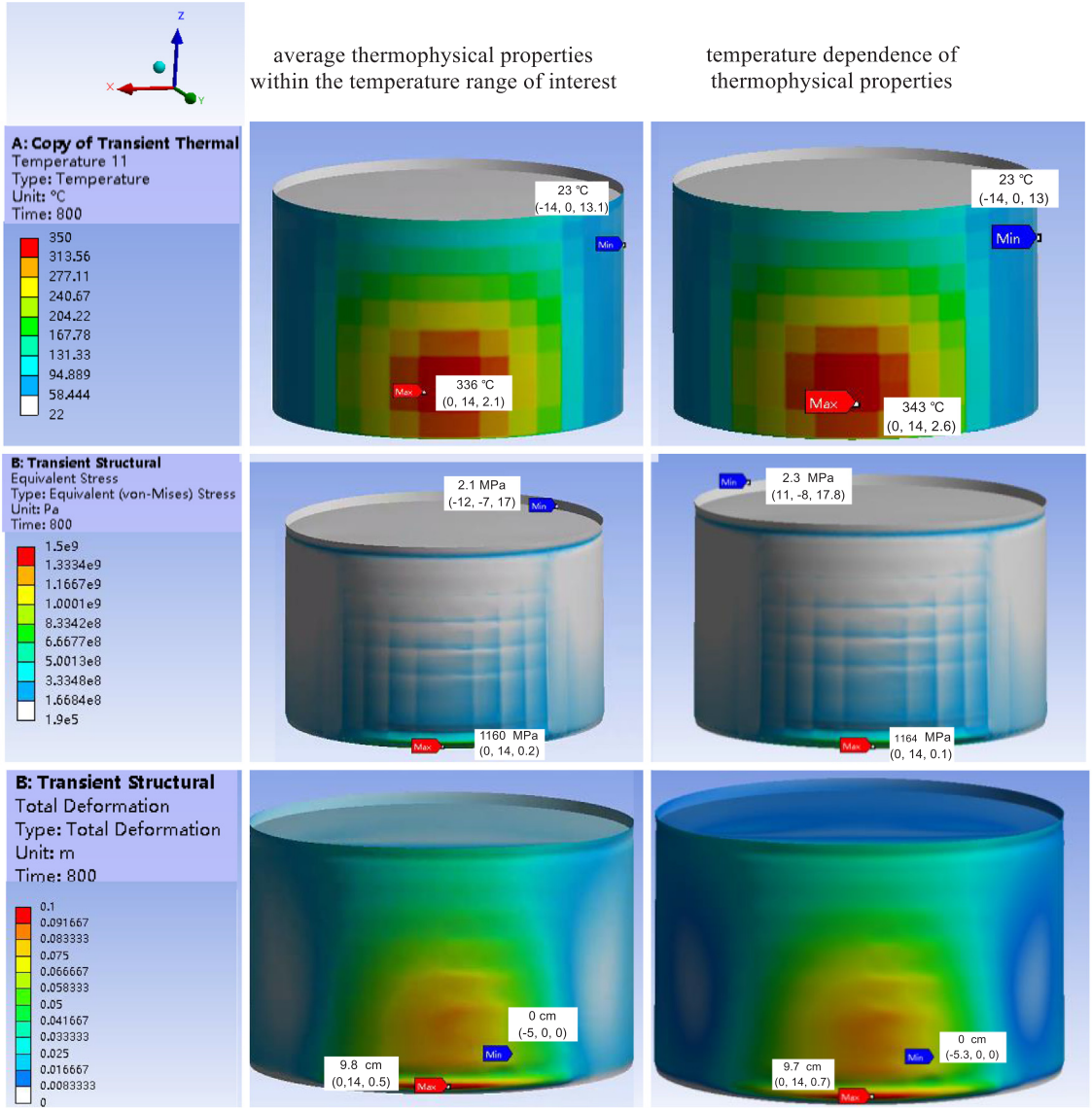

Fig. 10. . Temperature, equivalent stress and total deformation distribution of target gasoline tank: (left) average and (right) temperature dependency of thermo-physical properties of liquid medium.

3.3. Thermo-physical properties of the product stored in the target tank

Fig. 4 shows the flow diagram of crude oil processing in which gasoline, benzene and heptane are important products. Gasoline can be used as fuel in an engine and as substitute for heating purposes in chemical and physical laboratories [42]. Benzene is a basic raw material for producing synthetic materials and daily necessities. Benzene is also known as a solvent for coatings and as a blending agent to increase gasoline's octane number in the refining sector [43]. Heptane can be used as a standard solvent for octane number determination and organic synthesis. Gasoline, benzene and heptane are generally stored in the floating-roof tank, due to high volatility. Therefore, floating-roof tanks that store gasoline, benzene and heptane are chosen for illustrative purposes, and the empty tank is also studied as a reference.

Figs. 5(a)-(c) show the variations of specific heat, thermal conductivity, and density versus temperature, respectively, for the gasoline, benzene and heptane. Their averaged values are also given within the temperature range of interest (initial to boiling temperatures). The average thermal diffusivity is calculated to be 6.57×10^{-8}, 7.78×10^{-8} and 6.30×10^{-8} m^2/s for the gasoline, benzene and heptane, respectively.

3.4. Geometric discretization (Grid division) of target tank

The 3D physical model of target tank is built and then injected into the ANSYS Workbench platform for mesh generation. Since the tank holds a large size in the whole but a thin wall, the empty tank can be considered as a shell unit when the mesh is automatically generated. The grid size is set to be 0.5 m for the empty tank simulation which generates 10,652 nodes and 10,596 units, and 0.25 m for the full-filled tank which generates 948,395 nodes and 990,137 units.

4. Results and discussion

4.1. Radiant heat flux distribution on the target tank surface

Eqs. (3)–(6), together with the thermo-physical properties in Table 1, can calculate the continuous, mean and intermittent flame heights versus combustion efficiency of the gasoline pool fire, as shown in Table 3. The flame emissivity and radiative fraction of gasoline pool

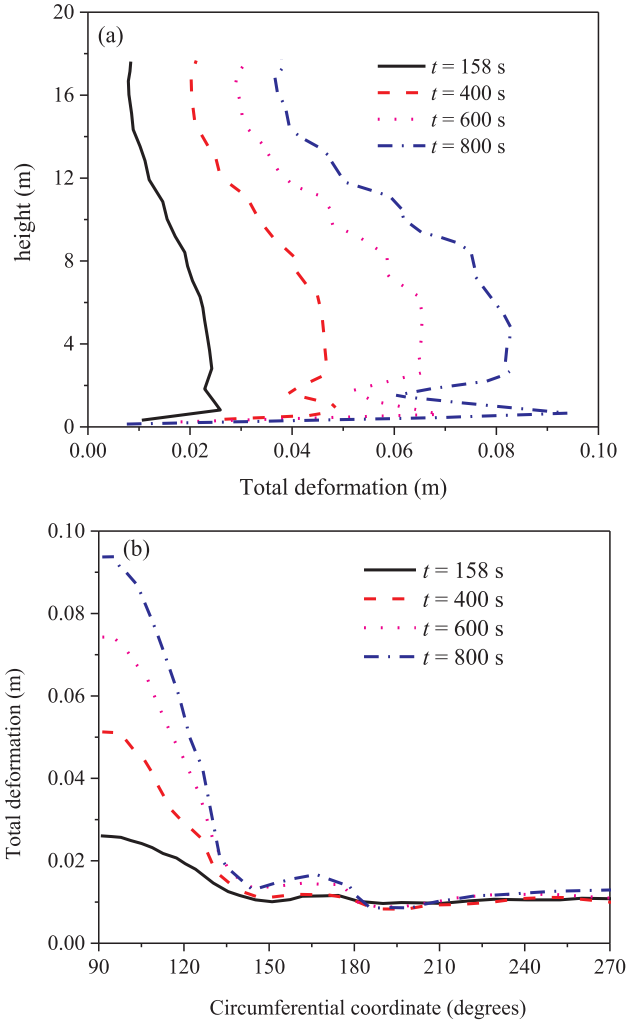

Fig. 11. . Total deformations of gasoline heated tank: (a) around the circumferential, (b) along the vertical directions.

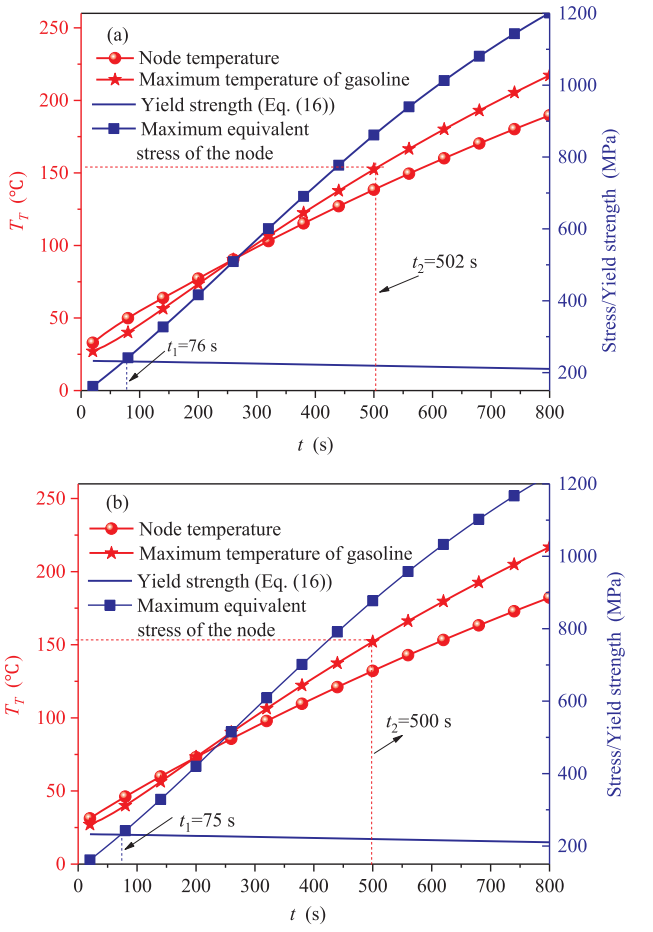

Fig. 12. Failure times related to thermal rupture and gasoline boiling of target tank: (a) average and (b) temperature dependency of thermo-physical properties.

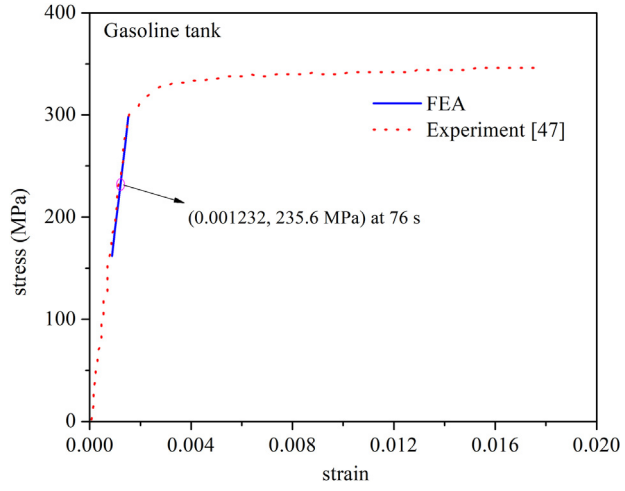

Fig. 13. Comparison of the strain-stress curve between numerical and experimental results.

fire are evaluated to be 1.0 and 0.086 by Eqs. (9) and (10), respectively. Accordingly, Eqs. (11) and (12) can determine the vertical profile of flame temperature under different combustion efficiencies with the calculated T_0 in Table 3. Application of the calculated pool fire parameters into Eq. (13) gives the radiant heat flux field received by the target tank.

Fig. 6 shows the radiant heat flux distribution on the target tank surface for the combustion efficiency of 0.2–0.8. As indicated, the gradient of radiant heat flux on the tank surface is considerably large. As the combustion efficiency increases, the heating area on the tank surface increases, while the maximum heat flux decreases. The combustion efficiency of heavy hydrocarbon pool fire ranges from 0.68 to 0.85 for the pool diameters of approximately 0.5–1.0 m [45], and the combustion efficiency decreases as the pool diameter increases [35]. The diameter of pool fire is 28 m in this paper, so the combustion efficiency of 0.4 will be used as a typical example for the following discussion.

Fig. 7 shows the radiant heat flux distribution on the top roof of target tank, and in the vertical and circumferential directions on the side surface. As shown in Fig. 7(a), the contours are getting denser as y increases on the top roof, which means the increase of radiant heat flux gradient as y increases. However, the contours firstly become denser and then sparser as x increases on the side surface, as shown in Fig. 7(b), showing that the gradient of radiant heat flux firstly increases and then decreases as x increases. In particular, the gradient of radiant heat flux reaches the maximum when the absolute value of x equals 10, as indicated by the zone A in Fig. 7(c), which is related to the sharp variation of geometric view factor. In short, the radiant heat flux increases, as the absolute value of x decreases and the y increases. The radiant heat flux firstly increases and then decreases as the z increases. That is to say, the maximum radiant heat flux appears at the position of (0, 14, 3.56) m. The distribution contour of radiant heat flux is

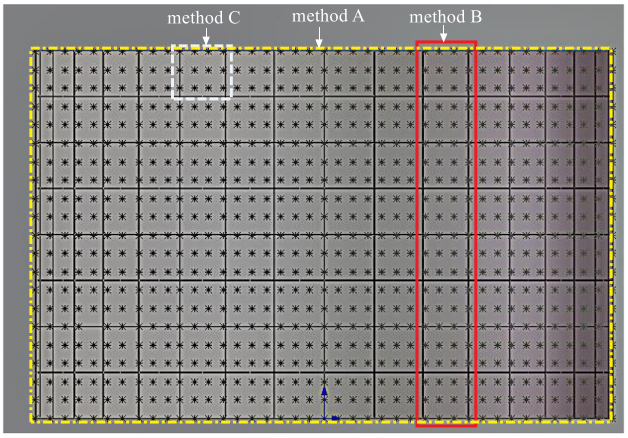

Fig. 14. Overall segmentation map of heated storage tanks.

symmetric around the plane of $x = 0$. Moreover, the calculated radiant heat flux should be loaded into the ANSYS Workbench platform for further thermal-structural coupling analysis.

4.2. Grid sensitivity analysis

The grid resolution is very important for the numerical simulation. A low grid resolution can lead to non-convergence or the calculation results of large errors, while a high one would consume a lot of computer resources. The case of empty tank is used to analyze the grid sensitivity of finite element simulation, by comparing the calculation results of different grid sizes. Fig. 8 shows the comparisons of the maximum temperature, total deformation and stress versus time between the grid sizes of 0.4 m, 0.5 m and 0.6 m. As shown, the temperature and total deformation are not sensitive to the grid size, while the equivalent stress of 0.6 m grid size deviates significantly from those of 0.4 m and 0.5 m grid sizes. The differences of calculation results are negligible between the grid sizes of 0.4 m and 0.5 m. Therefore, the grid size of 0.5 m is used for the empty tank, and the same method is also used to determine the grid size of 0.25 m for the full-filled tank, as stressed in Section 3.5.

4.3. Comparison of tank surface temperature: analytical prediction versus numerical simulation

The comparison is limited to the empty tank, for the theoretical calculation method in Section 2.3 is not valid for the full-filled tank. At the point where the maximum radiant heat flux locates, the temperature is calculated by the lumped capacitance method against the numerical simulation method. In particular, the heat transfer between the tank and surrounding air are assumed to be same in the outside and inner surfaces, as Eq. (14) is used for analytical prediction. Fig. 9 shows that the relative errors are less than 3% between numerical simulation and analytical prediction. Therefore, the numerical simulation shows a considerable accuracy.

The simulation time is 1800 s for the empty tank. However, the numerical simulation would cost much more resources for full-filled tank than empty one, if the simulation results keep the same accuracy. Accordingly, the simulation time should be shortened as reasonable as possible for full-filled tanks. In general, the failure time of target tank is about 500 s as the heat flux is 20 kW/m^2 received by the atmospheric pressure storage tank [46]. Since the maximum radiant heat flux is 36 kW/m^2 in this study, the numerical simulation of thermal-structural coupling analysis is performed for a total duration of 800 s.

4.4. Comparison between model calculations: average versus temperature dependency of thermo-physical properties of liquid medium

The available studies on the thermal behavior of tank exposed to fire, lack of consideration on the temperature dependency of thermo-physical properties of liquid medium in target tank. Zhao et al. [21] applied the constant thermo-physical properties, despite the increase of temperature due to the fire heating. Accordingly, it is necessary to quantify the effect of the constant thermo-physical property assumption on the simulation result of thermal response behavior. Comparison is conducted between the average and temperature dependency of thermo-physical properties within the temperature range of interest as detailed in Section 3.3.

Fig. 10 shows the temperature, equivalent stress and total deformation distribution of target tank. The left three pictures show the calculation results using the average thermo-physical properties of liquid medium within the temperature range of interest, while the right

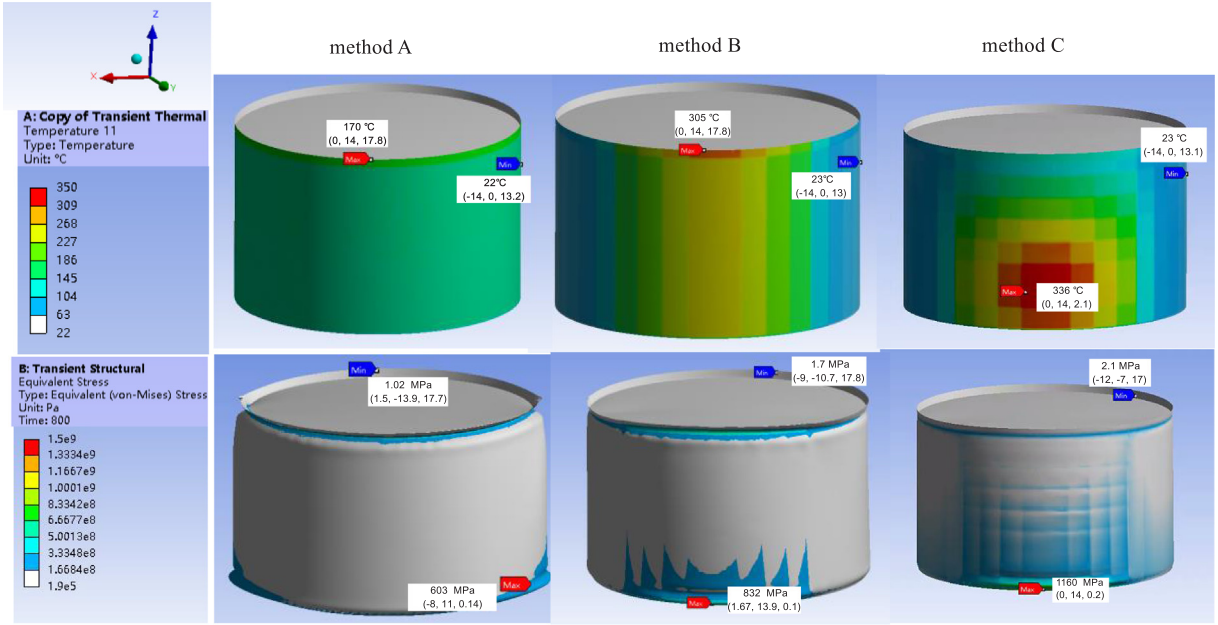

Fig. 15. Temperature and equivalent stress distribution on the target tank surface.

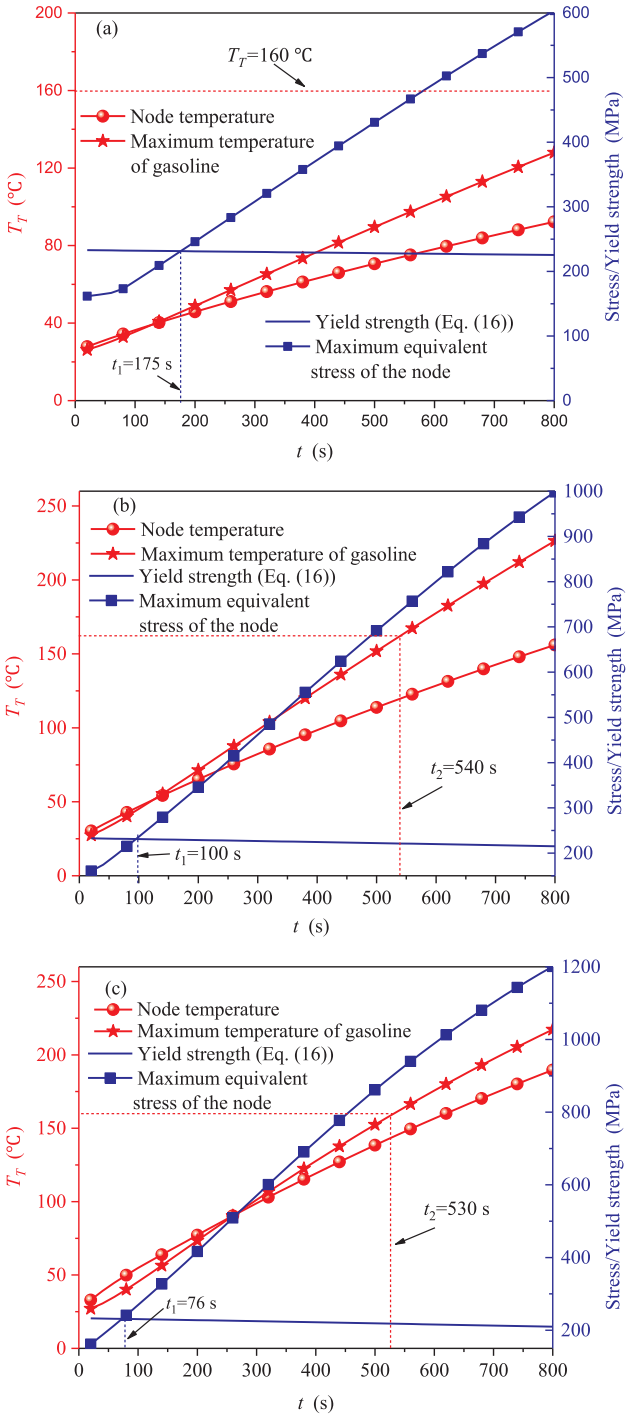

Fig. 16. The maximum temperature of gasoline, maximum stress and its corresponding temperature and yield strength calculated by the (a) method A, (b) method B and (c) method C.

ones are those using the temperature dependency of thermo-physical properties. The results show that the temperature, equivalent stress and total deformation distribution are almost the same for the both cases of thermo-physical properties. In particular, the maximum temperature, equivalent stress and total deformation appear at the same positions for both situations, respectively.

As clarified in Section 4.1, the maximum radiant heat flux locates at the position of (0, 14, 3.56) m. According to the energy conservation, the maximum temperature should also appear at the same position. The tank bottom base bears the whole weight of tank and fuel, and receives lots of radiant heat flux as compared to the tank top zone, causing a large temperature gradient nearby. Accordingly, the equivalent stress resulting from temperature gradient would be maximum near the tank bottom. Free thermal expansion related to the stress results in the deformation, and thus the maximum total deformation also appears near the tank bottom.

Fig. 11(a) presents the total deformation of the gasoline heated tank along the meridional direction where is the most heated zone. The heated tank has uneven displacement due to uneven temperature distribution. As shown, the total deformation increases as the time goes, while the tank bottom has less total displacement near the fixed bottom. The total deformation of lower-part is larger than the upper-part of the heated tank at t = 158 s, while the position of maximum total deformation would gradually move to upper-part, as the time increases. As the time goes, more and more folds appear on the tank wall, and thus the tank expands outward and deforms downward.

Fig. 11(b) presents the total deformation of the target tank around the circumference of the tank wall ($90° \leqslant \theta \leqslant 270°$) with z = 0.2 m where the failure point is involved, at typically different times. The deformation increases as the time increases. The deformation decreases sharply as θ increases from 90° to 140°, and then considerably fluctuates as θ increases from 140° to 180°, and finally almost maintains a constant as θ increases from 180° to 270°.

With the input of the temperature versus time calculated by numerical simulation, Eq. (16) can predict the transient decrease of yield strength of target tank. Accordingly, the failure time due to thermal rupture (t_1) can be determined by comparing the time profiles of equivalent Von Mises stress to the yield strength. The temperature versus time of liquid medium can also be given by numerical simulation, and comparison to boiling temperature can give the other failure time (t_2). Fig. 12(a) and (b) show the profiles of maximum equivalent stress and its corresponding temperature of tank wall, the corresponding yield strength and the maximum gasoline temperature, for the average and temperature dependency of thermo-physical properties, respectively, within the temperature range of interest. As shown, t_1 and t_2 are 76 s and 502 s using the average thermo-physical property, while they are 75 s and 500 s for temperature dependency of thermo-physical property. Thus, the constant thermo-physical property assumption holds little effect on the result of numerical simulation.

The failure time of 76 s with average thermo-physical property is obtained, and the strain-stress curve of FEA is compared with the experimental result. Experimental measurements were conducted on the stress-strain of Q235 under the temperature within the range of 293–1273 K [47]. As shown in Fig. 13, the FEA curve shows a good agreement with the experimental result.

4.5. Comparison between model calculations: uniform versus non-uniform radiant heat flux distribution on the target tank surface

As shown in Fig. 6, the radiant heat flux distribution is not uniformly distributed on the target tank surface, so that the temperature of tank wall should not be constant neither in the vertical nor in the circumferential directions. However, Zhang et al. [24] proposed an integrated probabilistic framework for tank farm optimal layout in which a constant radiant heat flux is applied to calculate the safety distance. Pantousa et al. [7] studied the thermal buckling behavior of fixed-roof tanks by assuming the constant temperature in the vertical direction of target tank. Thus, it is necessary to quantify the effect of the simple methods to load heat flux.

Fig. 14 shows three different methods to load the radiant heat flux into the ANSYS Workbench platform. In the method A, the radiant heat flux is constant on the front half of the target tank, and the average radiant heat flux is often used. In the method B, the radiant heat flux is constant in the vertical direction by averaging the calculation of different positions on the narrowly vertical surface, so it only varies in the circumferential direction. The last method C divides the tank wall into

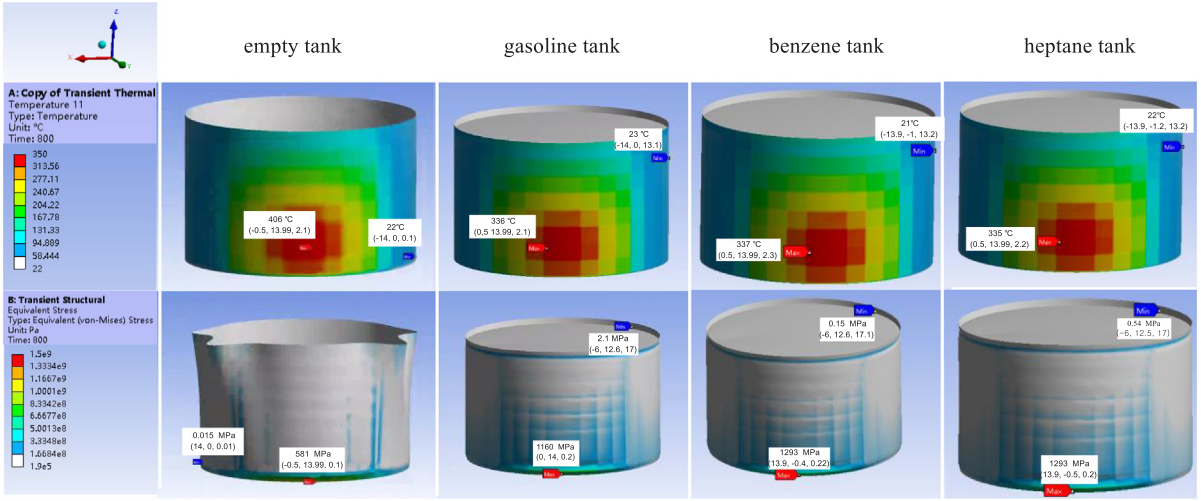

Fig. 17. Temperature and equivalent stress distribution on the surface of empty, gasoline, benzene and heptane tanks.

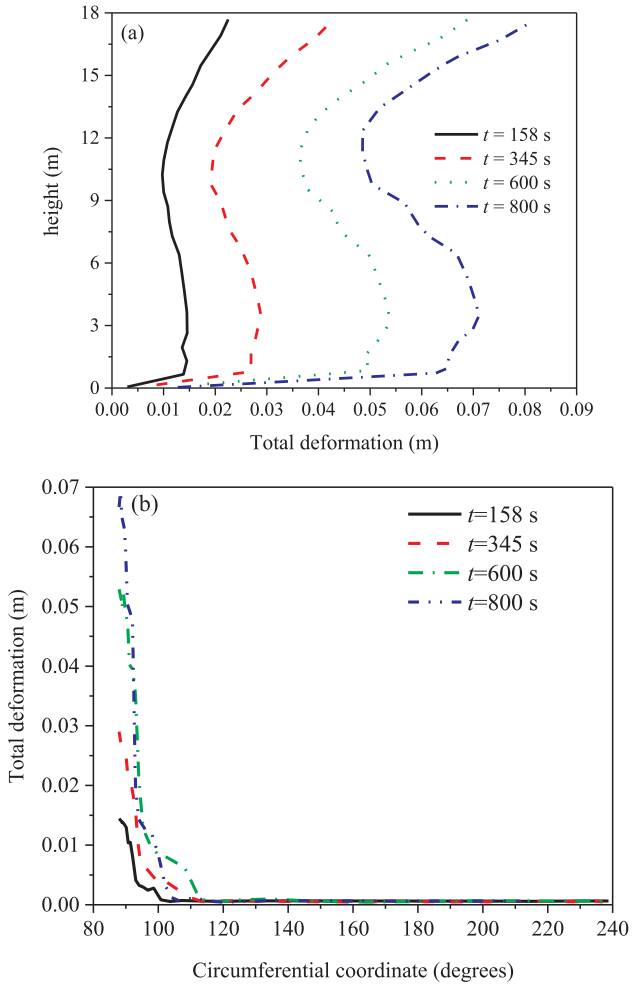

Fig. 18. Total deformations of empty tank (a) along the vertical directions and (b) around the circumferential of target tank.

cell surfaces and takes the average radiant heat flux in each cell surface, so the radiant heat flux varies in both vertical and circumferential directions. The methods A-C are adopted to load the radiant heat flux, in order to quantify the importance of considering the non-uniform radiant heat flux distribution on the target tank surface.

Fig. 15 shows the temperature and equivalent stress distribution of target tank. The left two pictures show the calculation results using method A, and the middle and right ones are those predicted by methods B and C, respectively. The results show that the method to load radiant heat flux holds a significant effect on the temperature and equivalent stress distribution of tank wall. The maximum temperature is 170 °C, 305 °C and 336 °C for methods A-C, respectively, while the maximum equivalent stress is 603 MPa, 832 MPa and 1160 MPa in turn. Thus, the load method significantly influences the positions where the maximum and minimum equivalent stresses locate, even though it little affects the positions of maximum and minimum temperatures.

Figs. 16(a)-(c) show the profiles of maximum equivalent stress and its corresponding temperature of tank wall, the corresponding yield strength and the maximum gasoline temperature using methods A-C, respectively. As shown, t_1 and t_2 are 175 s and over 800 s by method A, while they are 100 s and 540 s for method B, and 76 s and 530 s for method C. The failure time should be the minimum between t_1 and t_2, as discussion in Section 2.5. Thus, the failure time of gasoline tank is 175 s, 100 s and 76 s for methods A-C, respectively. Accordingly, the calculation result would overestimate the failure time and underestimate the fire risk in the previous studies [7,24].

4.6. Comparison of model calculations: effect of target tank filling (empty or storing liquid)

Fig. 17 presents the temperature and equivalent stress distribution of target tank for empty tank and full-filled tanks of gasoline, benzene and heptane. The results show that the tanks almost hold the same temperature and equivalent stress distributions, except the empty tank. The maximum temperature of the empty tank is larger than that of full-filled tanks, and the tank surface area of over 406 °C in temperature is much larger for empty tank than full-filled tanks. It indicates a lot of heat transferred from the tank wall to the storing liquid, for the convective heat transfer coefficient between the tank wall and the air is lower than that between the tank wall and storing liquid. In addition, a horizontal demarcation line appears in the circumferential direction across which there is a large temperature gradient, and the height of demarcation line is the same as that of liquid medium in tank.

For the empty tank, the floating roof locates at the bottom, so the upper part is open without any fixed constraint. Thus, the fixed constraint in the tank bottom produces the maximum equivalent stress in the lower part of the tank. In comparison, the maximum and minimum equivalent stress locate in the lower and upper part of full-filled tanks, respectively.

Figs. 18(a) and (b) present the total deformations of the empty tank along the meridional direction where is the most heated zone and

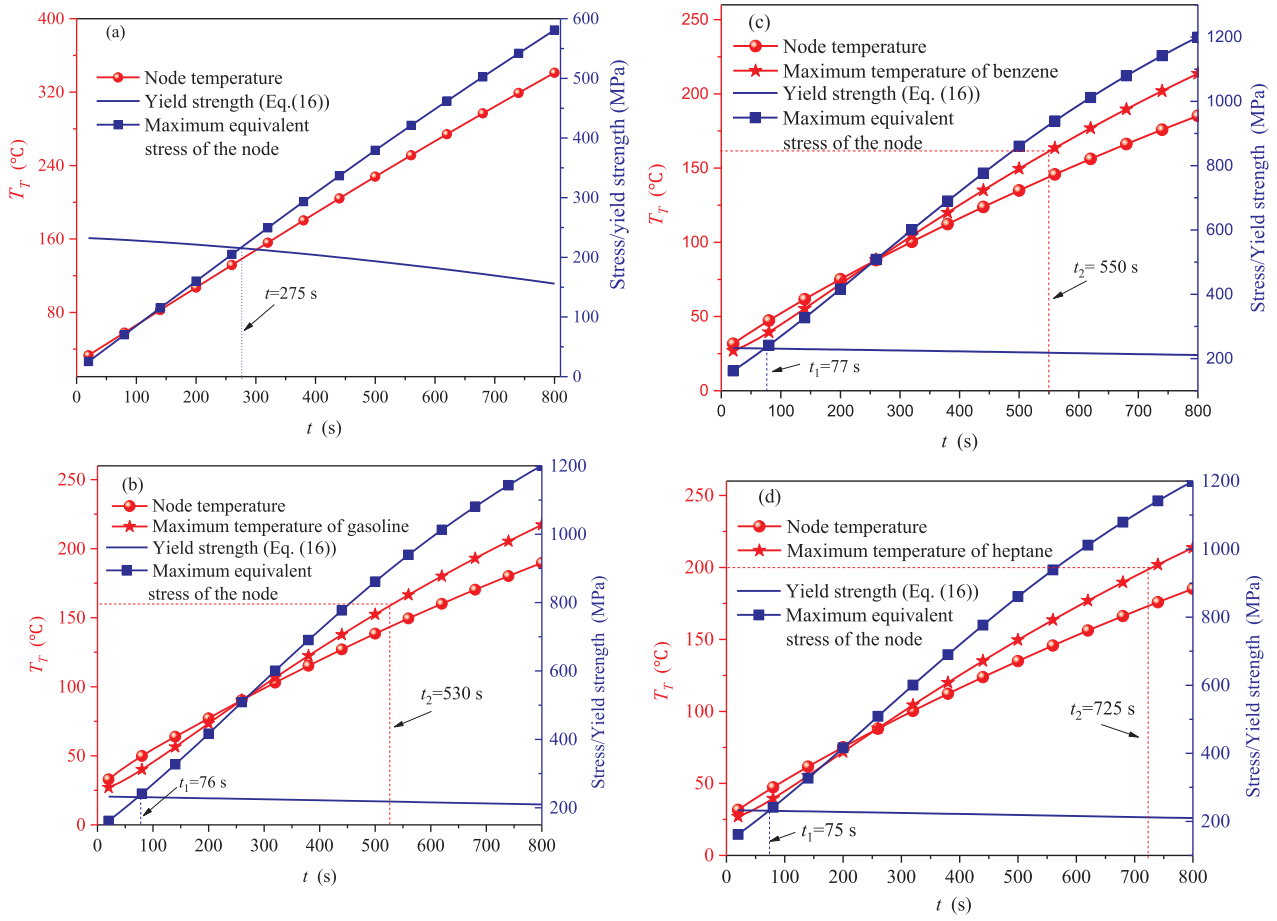

Fig. 19. The maximum temperature of liquid medium, maximum stress and its corresponding temperature and yield strength for the (a) empty, (b) gasoline, (c) benzene and (d) heptane tanks.

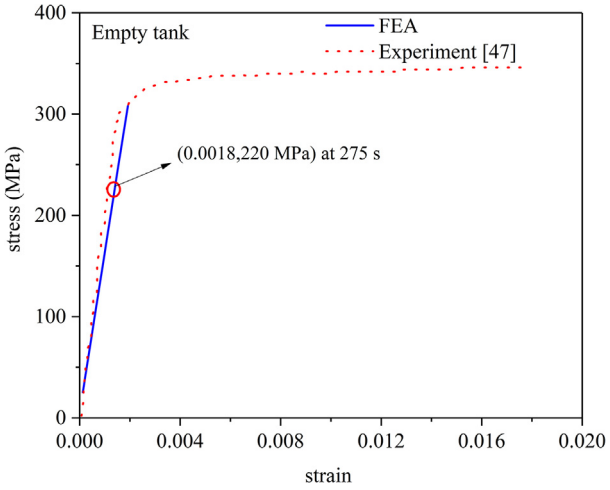

Fig. 20. Comparison of the strain-stress curve between numerical and experimental results.

around the circumference with $z = 0.2$ m where the failure point appears, respectively. Comparison between Figs. 11 and 18 clarifies the difference of total deformation between empty and full-filled tanks. In the vertical direction, the total deformation firstly increases and then decreases and finally increases with height for the empty tank, while it firstly increases sharply and then decreases and increases sharply and finally slowly decreases with height for the full-filled tank. Along the circumference direction, for the empty tank, the total deformation intensely decreases as θincreases from 90° to 110°, and almost maintains zero as θ increases from 110° to 270°. In comparison, the total deformation smoothly decreases as θincreases from 90° to 140°, and then holds a fluctuate transition to be a constant as θ increases from 140° to 270°, for the full-filled tank.

Figs. 19(a)-(d) show the time profiles of maximum equivalent stress and its corresponding temperature of tank wall, as well as the corresponding yield strength for empty, gasoline, benzene and heptane tanks, respectively. The maximum temperature of liquid medium is also given for the full-filled tanks. The results show that the failure time for empty tank is 275 s, while for fuel-filled tank, it is 76 s, 78 s and 75 s for the benzene, gasoline and heptane, respectively. Note that the air holds a larger thermal diffusivity than liquid medium, and that the thermal diffusivity shows a little decrease from benzene, gasoline to heptane (see Section 3.3). Accordingly, the failure time seems to increase with the increase of the thermal diffusivity of liquid medium in tank.

Fig. 20 shows the comparison of the strain versus stress between FEA and experimental measurement, for the empty tank. Note the failure time of 275 s for the empty tank. The good agreement of FEA with experimental measurement further validates the robustness of the theoretical framework proposed in this paper.

5. Conclusions

In this paper, a theoretical framework coupling pool fire dynamics model, multi-layer cylindrical flame radiation model, thermal-structural coupling analysis and the failure time correlation, is presented to investigate the thermo-mechanical response of floating-roof tanks exposed to a pool fire. The distribution fields of radiant heat flux,

temperature, equivalent stress and total deformation are calculated for the target tank. In particular, the proposed framework considers the effects of the temperature dependency of thermo-physical property, the non-uniform distribution of heat flux and the type of liquid medium. The major conclusions include:

(1) In model calculation, the thermo-physical properties of liquid medium in target tank can use the average within the temperature range of interest, even though they are functions of temperature.
(2) The calculation results would significantly deviate from the exact solutions and underestimate the fire risk, in case the simple methods available in existing literature, is adopted to treat the non-uniform distribution of radiant heat flux on the surface of target tank.
(3) The failure time of target tank depends on the thermal rupture of tank shell rather than the boiling of liquid medium in tank, and increases as the thermal diffusivity of medium increases. The failure time of empty tank is much larger than that of full-filled storage tank, due to the larger thermal diffusivity of air.

Declaration of Competing Interest

The authors declare that they have no known competing financial interests or personal relationships that could have appeared to influence the work reported in this paper.

Acknowledgements

This work was financially supported by the National Key R&D Program of China (No. 2016YFC0800100), and the National Natural Science Foundation of China under Grant Nos. 51876088 and 51834007. KZ acknowledges the support from the Six Talent Peaks Project of Jiangsu Province of China under Grant no. XNYQC-005 and China Scholarship Council under Grant no. 201908320209.

References

[1] K. Zhou, J. Jiang, X. Zhang, Flame pulsation-based model for predicting radiant heat flux of pool fire, J. Nanjing Tech Univ. (Natural Science Edition) 38 (2016) 114–118.
[2] A.T. Abdolhamidzadeh, B.D. Rashtchian, S.A. Abbasi, Domino effect in process-industry accidents – an inventory of past events and identification of some patterns, J. Loss Prev. Process Ind. 24 (2011) 575–593.
[3] C.C. Lin, J.I. Chang, A study of storage tank accidents, J. Loss Prev. Process Ind. 19 (2006) 51–59.
[4] J.C. Batista-Abreu, L.A. Godoy, M. Asce, Thermal buckling behavior of open cylindrical oil storage tanks under fire, J. Perform. Constr. Facil 27 (2013) 89–97.
[5] Q.Z. Liu, X.Q. Lang, Considerations on a fire and explosion accident at buncefield oil storage depot in England, Petrochem. Safety Environ. Protect. Technol. 25 (2009) 45–48.
[6] C.A. Burgos, J.C. Batista-Abreu, H.D. Calabró, R.C. Jaca, L.A. Godoy, Buckling estimates for oil storage tanks: effect of simplified modeling of the roof and wind girder, Thin-Walled Structures 91 (2015) 29–37.
[7] T.K. Pantousa D, M.A. Kefaki, Thermal buckling behavior of unstiffened and stiffened fixed-roof tanks under non-uniform heating, Journal of Constructional Steel Research, 143 (2018) 162-179.
[8] W.Y. Liu, C.H. Chen, W.T. Chen, C.M. Shu, A study of caprolactam storage tank accident through root cause analysis with a computational approach, J. Loss Prev. Process Ind. 50 (2017) 80–90.
[9] J. Casal, R.M. Darbra, Analysis of past accidents and relevant case-histories, Domino Effects in the Process Industries (2013) 12–29.
[10] N.J. Hoff, C.C. Chao, W.A. Madsen, Buckling of a thin-walled circular cylindrical shell heated along an axial strip, J. Appl. Mech. 31 (1964) 253.
[11] A.D. Aulisa, A. Tugnoli, V. Cozzani, G. Landucci, A.M. Birk, CFD modeling of LPG vessels under fire exposure conditions, Am. Inst. Chem. Eng. 60 (2014) 4292–4305.
[12] S.M. Tauseef, T. Abbasi, V. Pompapathi, S.A. Abbasi, Case studies of 28 major accidents of fires/explosions in storage tank farms in the backdrop of available codes/standards/models for safely configuring such tank farms, Process Saf. Environ. Prot. 120 (2018) 331–338.
[13] R. Tschirschwitz, D. Krentel, M. Kluge, E. Askar, K. Habib, H. Kohlhoff, S. Krüger, Experimental investigation of consequences of LPG vehicle tank failure under fire conditions, J. Loss Prev. Process Ind. 56 (2018) 278–288.
[14] G.E. Scarponi, G. Landucci, F. Heymes, V. Cozzani, Experimental and numerical study of the behavior of LPG tanks exposed to wildland fires, Process Saf. Environ. Prot. S0957582017304160 (2017).
[15] B. Zhao, The application of super wavelet finite element on temperature–pressure coupled field simulation of LPG tank under jet fire, Heat Mass Transf. 51 (2015) 231–237.
[16] L. Shi, J. Shuai, K. Xu, Fuzzy fault tree assessment based on improved AHP for fire and explosion accidents for steel oil storage tanks, J. Hazard. Mater. 278 (2014) 529–538.
[17] A. Rebec, P. Plešec, J. Kolšek, Pool fire accident in an aboveground LFO tank storage: thermal analysis, Fire Saf. J. 67 (2014) 135–150.
[18] D. Wang, P. Zhang, L. Chen, Fuzzy fault tree analysis for fire and explosion of crude oil tanks, J. Loss Prev. Process Ind. 26 (2013) 1390–1398.
[19] L.A. Godoy, J.C. Batista-Abreu, Buckling of fixed-roof aboveground oil storage tanks under heat induced by an external fire, Thin-Walled Structures 52 (2012) 90–101.
[20] Y. Li, J. Jiang, Q. Zhang, Y. Yu, Z. Wang, H. Liu, C. Shu, Static and dynamic flame model effects on thermal buckling: Fixed-roof tanks adjacent to an ethanol pool-fire, Process Saf. Environ. Prot. 127 (2019) 23–35.
[21] J.L. Zhao, H. Huang, K.S. Qu, B.N. Su, Research on thermal radiation response of large crude oil tank based on numerical simulation method, J. Central South University (Science and Technology) 48 (2017) 245–252.
[22] Y. Liu, Thermal buckling of metal oil tanks subject to an adjacent fire, The University of Edinburgh, Scotland, U K, 2011.
[23] K. Zhou, X. Wang, Thermal radiation modelling of pool fire with consideration on the nonuniform temperature in flame volume, Int. J. Therm. Sci. 138 (2019) 12–23.
[24] M. Zhang, Z. Dou, L. Liu, J. Jiang, L. Ni, Study of optimal layout based on integrated probabilistic framework (IPF): Case of a crude oil tank farm, J. Loss Prev. Process Ind. 48 (2017) 305–311.
[25] X. Lang, Q. Liu, H. Gong, Study of fire fighting system to extinguish full surface fire of large scale floating roof tanks, Procedia Eng. 11 (2011) 189–195.
[26] Y. Meng, D. Zhao, Y. Liu, W. Wang, Study on performance-based safety spacing between ultra-large oil tanks, Process Saf. Prog. 31 (2012) 398–401.
[27] J. Guan, J. Fang, D. Zhang, J. Wang, Y. Zhang, Experiment study of oil tank fire characteristics dependent on the opening of tank top, Procedia Eng. 62 (2013) 932–939.
[28] M. Jiang, ANSYS Workbench 19.0 basic introduction and engineering practice, Post & Telecom Press, Beijing, 2019.
[29] G. Heskestad, On Q* and the dynamics of turbulent diffusion flames, Fire Saf. J. 30 (1998) 215–227.
[30] E.E. Zukoski, Visible structure of buoyant diffusion flames, Symp. (Int.) Combust. 20 (1984) 361–366.
[31] P. Wang, N. Liu, Y. Bai, L. Zhang, K. Satoh, X. Liu, An experimental study on thermal radiation of fire whirl, Int. J. Wildland Fire 26 (2017) 693–705.
[32] V.C. Raj, S.V. Prabhu, A refined methodology to determine the spatial and temporal variation in the emissivity of diffusion flames, Int. J. Therm. Sci. 115 (2017) 89–103.
[33] E. Planas-Cuchi, J.M. Chatris, C. López, J. Arnaldos, Determination of flame emissivity in hydrocarbon pool fires using infrared thermography, Fire Technol. 39 (2003) 261–273.
[34] D. Burgess, A. Strasser, J. Grumer, Diffusive burning of liquid fuels in open trays, Fire Research Abstract and Revision 3 (1961) 91–106.
[35] J.C. Yang, A. Hamins, T. Kashiwagi, Estimate of the effect of scale on radiative heat loss fraction and combustion efficiency, Combust. Sci. Technol. 96 (1994) 183–188.
[36] K.B. McGrattan, H.R. Baum, A. Hamins, Thermal radiation from large pool fires, Gaithersburg, MD, USA, National Institute of Standards and Technology, 2000, p. 35.
[37] B.J. McCaffrey, Purely buoyant diffusion flames: some experimental results, National Bureau of Standards, Washington, D.C., 1979.
[38] T.L. Bergman, A.S. Lavine, F.P. Incropera, D.P. Dewitt, Fundamentals of heat and mass transfer, eighth ed., Wiley, 2017.
[39] ECCS, European recommendations for the fire safety of steel structures, Elsevier Scientific publishing company, 1983.
[40] V. Babrauskas, Estimating large pool fire burning rates, Fire Technol. 19 (1983) 251–261.
[41] D. Dong, F. Yuan, Practical manual for pressure vessels and chemical equipment, Beijing, 2000.
[42] J.R. Foster, The use of gasoline in chemical and physical laboratories, Nature 73 (1905) 29.
[43] Pure benzene will be serous short of supply, China Chemical Reporter (2007) 20–21.
[44] AP1700, Material property calculation platform, http://www.qp1700.com/ShowDetaill.htm, 2014.
[45] Y.I. Liang, H.U.O. Ran, Z.H.A.N.G. Jing-yan, L.I. Yuan-zhou, He-ping ZHANG. Characteristics of heat release rate of diesel oil pool fire, J. Combustions Sci. Technol. 02 (2006) 72–76.
[46] V. Cozzani, G. Gubinelli, E. Salzano, Escalation thresholds in the assessment of domino accidental events, J. Hazard. Mater. 129 (2006) 1–21.
[47] F. Ding, Z. Yu, H. Wen, Experimental research on mechanical properties of Q235 steel after high temperature treatment, J. Build. Mater. 02 (2006) 245–249.